Title	Uniquely selected primary dendrite arm spacing during competitive growth of columnar grains in Al-Cu alloy
Author(s)	Lee, Jaehoon; Ohno, Munekazu; Shibuta, Yasushi et al.
Citation	Journal of crystal growth, 558, 126014 https://doi.org/10.1016/j.jcrysgro.2020.126014
Issue Date	2021-03-15
Doc URL	https://hdl.handle.net/2115/88256
Rights	©2021. This manuscript version is made available under the CC-BY-NC-ND 4.0 license http://creativecommons.org/licenses/by-nc-nd/4.0/
Rights(URL)	https://creativecommons.org/licenses/by-nc-nd/4.0/
Type	journal article
File Information	2020Lee_manuscript_PDAS-GB_HUSCAP.pdf

Uniquely selected primary dendrite arm spacing during competitive growth of columnar grains in Al–Cu alloy

Jaehoon Lee[1], Munekazu Ohno[2,*], Yasushi Shibuta[3], Tomohiro Takaki[4]

[1] *Graduate School of Engineering, Hokkaido University, Kita 13 Nishi 8, Kita-ku, Sapporo, Hokkaido 060-8628, Japan*

[2] *Faculty of Engineering, Hokkaido University, Kita 13 Nishi 8, Kita-ku, Sapporo, Hokkaido 060-8628, Japan*

[3] *Department of Materials Engineering, The University of Tokyo, 7-3-1 Hongo, Bunkyo-ku, Tokyo 113-8656, Japan*

[4] *Faculty of Mechanical Engineering, Kyoto Institute of Technology, Matsugasaki, Sakyo-ku, Kyoto 606-8585, Japan*

*Corresponding author: mohno@eng.hokudai.ac.jp

Abstract

The steady-state value of primary dendrite arm spacing (PDAS) in the columnar dendrites growing between the converging and diverging grain boundaries is investigated by means of quantitative phase-field simulations. The simulations show that there is a unique value of PDAS under a given solidification condition in the system with grain boundaries. This is in contrast to existence of allowable range of PDAS under a given solidification in a system without the grain boundaries, i.e., an infinitely large columnar grain investigated in many early works. Such a unique value of PDAS depends on the pulling speed and inclination angle of the crystal, but not on the initial condition; that is, it is independent of the history of solidification condition. The dependences of the unique value on the pulling speed and inclination angle qualitatively agree with the theoretical models.

Keywords

A1. Computer simulation; A1. Dendrites; A1. Directional solidification; A1. Crystal morphology

1. Introduction

Columnar dendrites develop in the direction opposite to heat flow during directional solidification of alloys. Because their size, morphology, and crystal orientation strongly influence the quality of a cast [1, 2], it is essential to understand and control their growth processes. One of the important factors characterizing a columnar dendrite structure is primary dendrite arm spacing (PDAS), which is closely related to permeability in the mushy zone [3–6], as well as micro- and macro-segregation [6–8]. Thus, PDAS prediction is among the key issues in the field of solidification science.

Hunt [9] and Kurz and Fisher [10] proposed theoretical models to describe PDAS for different cooling conditions and alloy systems. These models are successful in qualitatively explaining the experimental results [11, 12]. Meanwhile, Warren and Langer discussed the dependence of PDAS on the history of microstructure and the solidification condition [13]. It is known that PDAS has an allowable range in a given condition. Furthermore, Hunt and Lu proposed analytical expressions for calculating PDAS, as well as cell spacing [14]. However, although the usefulness of these expressions has been well acknowledged, the improvement of the prediction accuracy remains an important issue to be addressed [15–17].

The phase-field model has emerged as a viable tool for predicting the formation of solidification structures [5, 18–25], in particular, with the recent development of the quantitative phase-field models [26–31], along with the progressive escalation of a high-performance computational technique [32, 33]. It is currently possible to conduct a large-scale quantitative analysis of dendritic structures [18–20, 22–25, 34-36]. For example, Gurevich et al. [19] investigated the allowable range of PDAS [20] in given solidification conditions and showed the behavior of the selection of PDAS influenced by the solidification history [19]. It is important to note that most of the previous studies have focused on the growth of single grains, i.e., a system without the grain boundary. In addition, the preferential growth direction of dendrites has often been fixed to the direction parallel to the temperature gradient. In reality, the competitive growth of columnar dendrites with different crystallographic orientations takes place, and, accordingly, the grain boundaries form between them. One of the interesting characteristics in this competitive growth of columnar dendrites with different inclination angles is the existence of the source and the sink of a new primary dendrite (or cell), which correspond to the diverging and converging grain boundaries [21, 22, 25, 37]. The new primary arm appears from the diverging grain boundary and then grows away from it. Tourret et al. [22] studied the behavior of PDAS in such a condition by changing the inclination angle by quantitative phase-field simulations and found that PDAS increases with increase in the inclination angles, as described by the model proposed by Gandin et al. [37]. Moreover, Song et al. [25] investigated the dynamical adjustment of PDAS in columnar dendrites growing between the diverging (source) and converging (sink) grain boundaries from transient to steady state of uniform distribution of PDAS. They proposed a theoretical model to describe the time evolution of spatial distribution of PDAS until steady state is

realized. A further investigation should be aimed at clarifying the behavior of steady-state and uniform PDAS for different solidification conditions. It is especially important to clarify the effects of the grain boundaries and inclination angles on the steady-state behavior of PDAS.

Herein, we investigate PDAS behavior in the competitive growth of columnar dendrites between the diverging and converging grain boundaries by means of quantitative phase-field simulations. We direct our attention towards the allowable ranges of the steady-state values of PDAS for different solidification conditions and its history dependence.

2. Methods

2.1. Quantitative phase-field model

In this study, the quantitative phase-field model developed by Ohno and Matsuura [27] is utilized to investigate the directional solidification [21, 38]. The phase-field variable ϕ takes $+1$ in solids and -1 in liquids and varies between these values continuously in the solid–liquid interface. The time evolution of ϕ is described by

$$\tau_0 a_s(\mathbf{n})^2 [1 - (1 - k)u'] \frac{\partial \phi}{\partial t} = W_0^2 \nabla \cdot [a_s(\mathbf{n})^2 \nabla \phi] + W_0^2 \frac{\partial}{\partial x}\left[a_s(\mathbf{n}) \frac{\partial a_s(\mathbf{n})}{\partial \phi_x} |\nabla \phi|^2\right]$$

$$+ W_0^2 \frac{\partial}{\partial y}\left[a_s(\mathbf{n}) \frac{\partial a_s(\mathbf{n})}{\partial \phi_y} |\nabla \phi|^2\right] - \frac{df(\phi)}{d\phi} - \lambda \frac{dg(\phi)}{d\phi}(u + u'), \tag{1}$$

where ϕ_x and ϕ_y are the spatial derivatives of ϕ in the x- and y-directions, i.e., $\partial \phi/\partial x$ and $\partial \phi/\partial y$, respectively. τ_0 is the phase-field relaxation time given by $\tau_0 = a_2 \lambda W_0^2/D_l$ with $a_2 = 0.6267$, interface thickness W_0, and solute diffusivity D_l. λ is the coupling constant expressed as $\lambda = a_1 W_0/d_0$ with $a_1 = 0.8839$ and the capillary length d_0. $a_s(\mathbf{n}) = 1 - 3\varepsilon + 4\varepsilon(\phi_x^4 + \phi_y^4)/|\nabla \phi|^4$ is the anisotropy function with anisotropy parameter ε. As for interpolation functions, we chose $df(\phi)/d\phi = -\phi + \phi^3$ and $dg(\phi)/d\phi = (1 - \phi^2)^2$. u is the dimensionless supersaturation defined by $u = (c_l - c_l^e)/(c_l^e - c_s^e)$, where c_l is the liquid concentration, and c_l^e and c_s^e are the equilibrium concentrations of the liquid and solid phases. u' is the additional supersaturation associated with the temperature. Meanwhile, the time change of the temperature T follows the frozen temperature approximation

$$T(y) = T_0 + G(y - V_p t), \tag{2}$$

where G indicates the temperature gradient along the y-axis, V_p is the pulling speed, and T_0 is the reference temperature, i.e., the temperature at $y = 0$ and $t = 0$. From this definition, $u' = (y - V_p t)/l_t$, where l_t is the thermal length defined by $l_t = |m|(1 - k)c_0/(kG)$ with the liquidus slope m, initial concentration c_0, and partition coefficient k.

The diffusion equation is given by

$$\frac{1}{2}[1 + k - (1 - k)\phi]\frac{\partial u}{\partial t} = \nabla[D_l q(\phi)\nabla u - j_{AT}] + \frac{1}{2}[1 + (1 - k)u]\frac{\partial \phi}{\partial t} - \nabla \cdot J, \tag{3}$$

where $q(\phi)$ is an interpolating function given by $q(\phi) = [kD_s + D_l + (kD_s - D_l)\phi]/(2D_l)$, D_s is the

diffusion coefficient in solid. Moreover, j_{AT} is the antitrapping current expressed as $j_{AT} = -(1 - kD_s/D_l)/(2\sqrt{2})W_0[1 + (1 - k)u](\partial\phi/\partial t)\nabla\phi/|\nabla\phi|$, where J is a fluctuating current.

2.2. Computational conditions for a two-dimensional (2D) system

We focused on the Al-3mass%Cu (0.013 at. frac.) alloy [1, 12, 17, 21, 38]. The simulations were mostly conducted in a 2D system, under the initial condition schematically shown in Fig. 1. The spatial grid spacings Δx and Δy were set at $\Delta x = \Delta y = 0.5$ μm, based on a balance between the accuracy and computational cost, found in the preliminary simulations. The size of the computational system was set at $L_x \times L_y = 3008\Delta x \times 1536\Delta y$ (= 1.504 mm $\times$ 0.768 mm). Initial seeds of solid were equally spaced at the bottom of the system as Fig. 1 (a). Moreover, the spacing between the seeds, called here as initial PDAS λ_0, was varied from 0 to 215 μm. When $\lambda_0 = 0$ μm, the initial solid is thin plate as shown in Fig. 1 (b). G was fixed at 30 K/mm, and V_p was changed from 60 to 200 μm/s. The inclination angle θ, the angle between the y-direction and the [100] direction of the seed, was varied from 5° to 40°. Here, θ is positive when the [100] of solid rotates in the anticlockwise direction. Our main concern is the influence of the grain boundaries on the steady-state value of PDAS. We mainly focused on the symmetric grain boundaries at which the dendrites forming the grain boundary have the same absolute value of $|\theta|$ with the different signs. This growth process can be simulated by using the mirror boundary condition at the system edges where the grain boundaries exist. We set the boundary at the right-hand edge of the system as the diverging grain boundary and that at the left-hand edge the converging grain boundary. Moreover, we investigated the effects of an asymmetric diverging grain boundary on PDAS. More specifically, a seed of solid having an inclination angle θ^* was placed on the right-hand side of the seeds with θ, and these two types of seeds grow to be columnar dendrites forming the asymmetric diverging grain boundary. We investigated effects of θ^* on PDAS of dendrites with θ. We also investigated the growth without the grain boundary by applying the periodic boundary condition to both the edges of the system. We call the simulation without the grain boundary case 1. Also, the simulations for growth with symmetric and asymmetric grain boundaries are called case 2 and case 3, respectively, in this paper.

The parameters employed were indicated in table 1 [21, 23, 38]. The time step was set to $\Delta t = 1.65 \times 10^{-5}$ s, and the computations were stopped after 4×10^7 steps, which is equivalent to the solidification time of 660 s. All calculations were accelerated by using parallel computing on a TESLA P100 graphics processing unit and a moving-frame scheme.

2.3. Measurement of average PDAS λ_l in 2D system

When the grain boundary exists, PDASs are initially non-uniform as discussed in Ref. [25]. To understand the behavior of individual PDASs, we measured the distances between the growing tips of the neighboring dendrites, as shown in Fig. 2. Because the tip position of each dendrite slightly

moves or oscillates in the moving-frame calculation, the position slightly lower than the tip was used to calculate PDAS. Specifically, the position at $60\Delta x$ away from the highest tip of the dendrite was used. We confirmed that the choice of distance does not affect the result until it is close to the position where the branching of a secondary arm occurs. In this study, the average PDAS λ_1 was obtained by averaging the individual PDASs λ_i^L thus calculated. Note that the leftmost dendrite near the converging grain boundary was not included in the calculation of λ_1, because its tip position largely fluctuates due to overgrowth at the grain boundary.

2.4. Computational conditions for a three-dimensional (3D) system

For quantitative discussions, we performed 3D simulations for the growth of columnar dendrites in a thin plate sample. For computational efficiency, nonlinear preconditioning [39] was employed, and the spatial grid spacings Δx, Δy, and Δz were set to 0.8 μm, where Δz indicates the grid spacing for the *z*-direction. Note that there was only one row of dendrites in the thickness direction, i.e., the *z*-direction. In the preliminary calculation, we found that the tip positions of the dendrites do not change or oscillate largely in the *z*-direction but is located in the middle of the thickness of the thin plate system. Thus, we applied the mirror boundary condition on the *x*–*y* plane at $z = 0$ and dendrites of half-thickness were simulated. The length of *z*-direction L_z was chosen to be large enough to avoid the dependence of the results on L_z. More specifically, $L_z = 32$, 40, and $48\Delta z$ ($= 25.6$, 32.0, and 38.4 μm) were tested, but only the results for $L_z = 40\Delta z$ is shown in this study. The Neumann boundary condition was applied on the *x*–*y* plane at $z = L_z$, whereas the mirror boundary condition was applied on the *y*–*z* planes at $x = 0$ and L_x. Further, L_x and L_y were set at $L_x = L_y = 800\Delta x$ ($= 0.640$ mm), $V_p = 150$, 100, and 50 μm/s, and $\theta = 5°$. The rest of the parameters were the same as in the 2D simulations.

3. Results and Discussion

3.1. Effect of grain boundary on PDAS

Figure 3 shows the temporal evolution of columnar dendrites during directional solidification in systems (a) without and (b) with the grain boundaries, which corresponds to case 1 and case 2, respectively. The calculations were carried out for $V_p = 100$ μm/s, $\theta = 5°$, and $\lambda_0 = 0$ μm. In case 1, the competitive growth of columnar dendrites take place at an early period [Fig. 3(a1)]. After about 21 s, the tip positions of all dendrites are almost the same; however, individual PDASs λ_i^L are slightly non-uniform [Fig. 3(a2)]. PDASs become uniform after 168 s [Fig. 3(a3)], whereas the total number of columnar dendrites remains unchanged from that at 21 s [Fig. 3(a2)]. Therefore, in case 1, λ_1 take the steady-state value from the very beginning, with such a value essentially determined by the initial competitive growth process. In case 2, however, the behavior of PDAS is quite different. After the initial competitive growth [Fig. 3(b1)], the branching occurs at the diverging grain boundary (right-side edge), with a tertiary arm generated at this side growing to be a new primary arm as

indicated by the dotted circle [Fig. 3(b2)]. PDAS formed by the newly branched dendrite gradually decreases as it moves towards the left-side edge, i.e., the converging grain boundary. Moreover, the spatial distribution of PDASs in the columnar dendrites growing between the diverging and converging grain boundaries before the steady state was investigated in detail in the early work [25] and the present result in the early period shown in FIG. 3(b) is consistent with the finding of the work [25]. At 168 s [Fig. 3(b3)], all λ_i^L take almost the same value throughout the entire grain, and the steady state is achieved. Importantly, the values of λ_1 in the steady state in cases 1 and 2 are obviously different from each other. Such a difference was pointed out in the early work [25].

Figure 4(a) shows the time changes of λ_1 in case 1 for $\lambda_0 = 0$, 150, and 215 μm. When $\lambda_0 = 0$ μm, λ_1 reaches the steady-state value after an initial rapid increase and decrease. When $\lambda_0 = 150$ and 215 μm, λ_1 does not change from each initial value, indicating that λ_1 largely depends on λ_0. This is consistent with the early finding in the experimental and numerical works describing that the steady-state value of λ_1 is largely affected by the history of solidification condition [13, 15–17, 19, 40]. We systematically investigated the selected value of λ_1 in the steady state for different initial conditions by changing λ_0 and found that, for instance, when $V_p = 100$ μm/s, the lower and upper bounds of λ_1 were obtained from calculations for $\lambda_0 = 0$ mm and $\lambda_0 = 225$ mm, respectively. In this paper, the upper and lower limits of λ_1 obtained from different λ_0 will be called as the maximum and minimum values, respectively in case 1. However, in contrast with the existence of allowable ranges of PDAS in case 1, we observed a different behavior in case 2 where the grain boundaries exist. Figure 4(b) shows the results in case 2 for different values of λ_0. Note that λ_1 reaches the same steady-state values regardless of λ_0; thus, we could say that when there are grain boundaries, a unique value of λ_1 exists for a given solidification condition, which contradicts the result shown in Fig. 4(a). Meanwhile, the results for (a) $V_p = 80$ μm/s and (b) $V_p = 200$ μm/s in case 2 are shown in Fig. 5. Note that λ_1 attains a unique value for each value of V_p in the steady state regardless of λ_0. Also, the unique value decreases with an increase in V_p.

Figure 6 provides a summary of the dependence of the unique value of λ_1. Here, the horizontal axis is given by $c^{0.25} V_p^{-0.25} G^{-0.5}$, and the vertical axis is λ_1^T calculated from time averaging the values of λ_1 during the steady state (i.e., 300 to 660 s). Moreover, the minimum and maximum values of λ_1^T in the system without the grain boundary (case 1) are shown. The unique value is located in-between the minimum and maximum values. For comparison, the results of Hunt [9] and Kurz and Fisher [10] models are also shown. As could be seen, the slope of the unique value of λ_1^T with respect to the horizontal axis is slightly different from the theoretical models. Although not shown here, in case 1, the tip undercooling of columnar dendrites in the steady state ΔT_{tip} monotonically decreases as λ_1^T increases. ΔT_{tip} in case 2 is located on the $\Delta T_{tip} - \lambda_1^T$ curve obtained in case 1. As expected, therefore, the unique value of λ_1^T appear not as the most stable steady state but as a uniquely selected one. Such a selection is closely related to the branching at the diverging grain boundary and the growth processes

of the secondary and tertiary arms [Fig. 3(b)].

We found the aforementioned results for case 2 in the system with symmetric grain boundaries that were simulated by applying the mirror boundary condition. Because the emergence of a unique value of λ_1 is closely related to branching near the diverging grain boundary, we investigated the effects of an asymmetric diverging grain boundary (case 3) on λ_1. For this, another seed of solid having an inclination angle θ^* was placed on the right-hand side in the simulation, as shown in Fig. 7(a), where another dendrite is represented in yellow. Moreover, to prevent the elimination by the competing dendrites, the number of seeds were enlarged by changing L_x from 1.504 mm to 2.8 mm. Here, θ was fixed at $\theta = 5°$, whereas θ^* was varied. θ^* is positive when the dendrite rotates in the clockwise direction. Thus, the symmetric diverging grain boundary is realized when $\theta^* = 5°$. It is seen in Fig. 7(b) that λ_1^T does not depend on θ^*. Although the grain boundary orientation changes with θ^*, as detailed in the works [41, 42], such a change does not yield a significant difference in the unique value of λ_1^T. In the following subsection, we will focus on a system with symmetric grain boundaries realized by the mirror boundary condition, mainly because of its low computational cost.

3.2. Behavior until steady state

Figure 8(a–c) displays the time dependence of the individual PDAS λ_i^L for $V_p = 60$, 100, and 200 μm/s, respectively. All λ_i^L formed by dendrites that exist up to the steady state were numbered from the converging (left) to the diverging grain boundary (right). For this case, λ_0 was set to $\lambda_0 = 0$ μm. When the leftmost dendrite is eliminated at the converging grain boundary, the number of λ_i^L changes to the next one, leading to a sharp rise in λ_i^L. For instance, in Fig. 8(a), the PDAS specified as λ_6^L (bold purple line) turns smoothly into that specified as λ_5^L (blue line) at around 120 s, because of vanishment of the leftmost dendrite. Almost simultaneously, a new primary arm appears at the diverging grain boundary, and λ_6^L sharply increases to the value of this newly appearing PDAS. In all cases, λ_i^L are not uniform in the early periods. However, they become closely uniform after about 300, 160, and 80 s for $V_p = 60$, 100, and 200 μm/s, respectively, where their uniform values correspond to the unique values of λ_1^T. Also, in Fig. 8(a), all λ_i^L gradually decreases in the early periods (100 to 300 s), indicating that the dendrite closer to the diverging grain boundary rotated more to the anti-clockwise direction. As the rightmost dendrite grows and drifts to the left, the undercooled region is extended more around the diverging grain boundary. The dendrite newly developed by branching exhibits λ_6^L larger than that formed in the previous branching; that is, the value of λ_6^L would increase each time a new primary arm would develop from the diverging grain boundary in the early period. Accordingly, the uniform distribution with the unique value of λ_1^T is sequentially realized from the side of the diverging grain boundary. The similar behavior is observed in cases of $V_p = 100$ and 200 μm/s. In all cases, some PDASs especially near the diverging grain boundary fluctuates even in the steady state, whereas such a deviation rapidly settles into the unique value. When the newly developed PDAS was

smaller than the unique value, it gets larger by using the extra space left on the side of the diverging grain boundary. On the other hand, when it was larger than the unique value, it gets smaller through the lateral drift. The other PDASs uniformly maintain almost a constant value in the steady state.

It is seen in Fig. 8 that the time to reach the steady state obviously decreases as V_p increases from 60 to 200 μm/s. The similar trend is also found in Fig. 5. To elaborate this point, we investigated the solidification length to reach the steady state for different values of V_p. First, we found that the time to reach the steady state does not essentially depend on λ_0. Therefore, the time to reach the steady state can be estimated from the comparison between the behavior from different λ_0, as shown in Fig. 9(a) where the results for $\lambda_0 = 115$ and 215 μm are shown. These values of λ_0 result in the minimum and maximum λ_1 for $V_p = 100$ μm/s, respectively, in case 1. Both values of λ_1 gradually approach each other, and thus, the difference between them $\Delta\lambda$ gradually decreases. When $\Delta\lambda$ approaches a certain small value, we can consider that the steady state is realized. Once $\Delta\lambda$ is defined, the time and the solidification length required to reach the steady state can be calculated. The results of the time and the solidification length are shown in Fig. 9(b) and (c), respectively. Here, the black plots represent the average values of the calculated results of $\Delta\lambda = 5$, 10, 15, and 20 μm, and the error bar represents the results when $\Delta\lambda = 5$ and 20 μm. Although there are huge differences in time needed towards the steady state, the solidification length fall in the narrow range of 13–18 mm in all cases. As understood in Fig. 8, the frequency of branching at the diverging grain boundary increases with V_p; thus, λ_i^L close to the unique value of λ_1^T appears fast when V_p is large. However, the number of dendrites in a grain increases with V_p, implying that the number of dendrites that must appear at the diverging grain boundary to realize the uniform distribution of PDAS (i.e., the unique value of λ_1^T) would increase with V_p. The balance between these variables narrows the range of the solidification length required for the steady state.

As described in the introduction, Song et al. [25] investigated dynamical adjustment of spacings between the diverging and converging grain boundary from transient state to the steady state. The study in Ref. [25] described the mechanism of the propagation of spacings from generation of new spacing at the diverging grain boundary in detail. Importantly, they developed a model to describe the propagation velocity of spacing as follows,

$$V_\lambda \approx V_d(\lambda_p) - \left[\frac{dV_d}{d\lambda}\right]_{\lambda=\lambda_p} \lambda_p \tag{4}$$

where V_λ is the propagation velocity of spacing, V_d is given as $V_d = V_p \tan \alpha \approx V_p \alpha$ and λ_p is the characteristic value of PDAS. Here, α is the inclination angle of the growing direction of dendrite from the heat flow direction and it is given as $\alpha / \theta = 1 - 1 / (1 + f Pe^g)$ with $Pe = \lambda V_p / D$ and alloy-dependent constant f and g. Note that the time to reach steady state can be obtained by dividing the width of the system by V_λ. We calculated the time and the solidification length needed to become steady-state for each V_p based on Eq. (4). The results are indicated as the open square plots in Fig. 9

(b) and (c). The result of Eq. (4) is in a reasonable agreement with the present results.

Subsequently, to see the effect of grain size (L_x) on λ_1, we carried out simulations in the systems with $L_x = 2.368$ and 0.624 mm. The other conditions include $V_p = 100$ μm/s, $\theta = 5°$, and $\lambda_0 = 215$ μm. The results are shown in Fig. 10, where the blue-colored solid line is identical to the blue-colored dashed line in Fig. 4(b). When the grain size is small; i.e., $L_x = 0.624$ mm, λ_1 largely fluctuates, since there were small number of dendrites which can be significantly affected by the fluctuating value of newly developed PDAS at diverging grain boundary (Fig. 8). The fluctuation of λ_1 is not significant in the large grain of $L_x = 2.368$ mm, because PDAS was homogeneously distributed through the adjustment during the lateral drift. Importantly, λ_1 reaches almost the same steady-state value in all cases. Therefore, the unique value of λ_1 is independent of the grain size. Furthermore, the time to reach the unique value was shorter as the grain size is smaller. The number of dendrites is small in the small grain and, therefore, the number of dendrites that must appear to realize the uniform distribution of PDAS is small in the small grain. Therefore, the unique value of λ_1 is immediately realized in the small grain.

3.3. Rapid change of pulling speed V_p

Gurevich et al. [19] investigated the dependence of PDAS at the steady state on the initial condition and history of the solidification condition by means of the phase-field simulations. They focused on the directional solidification of Al–Cu alloy and a system without the grain boundary, i.e., case 1, and found that PDAS depends on the history of change of the pulling velocity. In this study, we investigated the history dependence of PDAS for a system with the grain boundaries (case 2), focusing on the steady-state value of PDAS at a given value of V_P realized by the rapid change of V_p from the different steady states. The behavior was examined under the following conditions: $200 \rightarrow 60 \rightarrow 200$ μm/s, $100 \rightarrow 200 \rightarrow 100$ μm/s, and $60 \rightarrow 100 \rightarrow 60$ μm/s. θ and λ_0 were fixed as $\theta = 5°$ and $\lambda_0 = 0$ μm. L_x was set to 0.768 mm in the light of low computational cost.

Figure 11(a) depicts the time change of λ_1 associated with the rapid change in V_p. In all cases, V_p is changed at 330 and 660 s, where λ_1 changes to the new steady-state value. The behavior of λ_1^T at the steady state is shown in Fig. 11(b). In all cases, λ_1^T was evaluated within 50–250, 450–650, and 750–950 s. Figure 11(b) shows that λ_1^T does not exhibit any dependence on the previous value of V_p, but attains a value unique to the given V_p, which could not be observed in the system without the grain boundary (case 1).

3.4. Effect of inclination angle θ on PDAS

To understand the effect of θ on λ_1, we systematically changed θ from 5° to 40° while keeping the rest of the computational condition the same as that described in Section III.A. Figure 12(a) and (b) represents the time changes of λ_1 calculated for different values of θ in cases 1 and 2,

respectively. In case 1, the steady-state value of PDAS is almost independent of θ when $\theta < 20°$, whereas it slightly increases when θ increases from 20° to 40°. In case 2, we could see that λ_1 largely depends on θ; in particular, it significantly fluctuates with time when θ is large. Figure 12(c) shows a snapshot of microstructure at 668 s for $\theta = 40°$ in case 2, in which there is a diverging grain boundary at the right-side edge. When θ is large, some tertiary branches simultaneously appeare at the diverging grain boundary; thus, λ_1 largely fluctuates with time.

Furthermore, in Fig. 13, we drew a comparison of the present values of λ_1^T for different θ with the values obtained from the model proposed by Gandin et al. [37] expressed as $\lambda_1 = LG^{-0.5}\{1 + d [\cos(\theta)^{-e} - 1]\}$. Here, L, d, and e are constants. The red-colored plots indicate the results of phase-field simulations for case 2, whereas the upward and downward triangular plots respectively indicate the maximum and minimum values calculated for case 1. The red-colored dashed line and dashed dot and dashed two-dot lines show the results by the model of Gandin et al.. These curves were obtained by fitting to the results of the phase-field simulations. The constants were obtained as $(L, d, e) = (0.027, 3.57, 0.79)$ in case 2, $(L, d, e) = (0.038, 2.12, 1.15)$ for the maximum value, and $(L, d, e) = (0.019, 0.97, 1.58)$ for the minimum value in case 1. The model can explain the dependence of λ_1 on θ in all cases.

3.5. Steady state in the 3D system

Although a 2D simulation is generally able to qualitatively reproduce the important aspects of the growth process of columnar dendrites in a thin sample, a 3D simulation is essential for a quantitative discussion. Figure 14(a) shows an example of dendrite structure in a 3D thin sample calculated for $V_p = 100$ μm/s at 270 s. The new primary arm was generated by branching at the diverging grain boundary. The time changes of λ_1 for different values of λ_0 at $V_p = 100$ μm/s and $\theta = 5°$ are shown in Fig. 14(b), where λ_1 approaches to the unique value despite of the different λ_0, which confirms the existence of the unique value of λ_1 in a 3D case. The unique value of λ_1 obtained in the 3D simulations is plotted as blue-colored squares in Fig. 6. We could see that the results of the 3D case are smaller than those of the 2D case. In the 3D case, furthermore, the slope of the unique value of λ_1^T with respect to the horizontal axis is consistent with the theoretical models.

4. Conclusion

PDAS is one of the important factors characterizing the columnar dendrite structure. It is known to exhibit an allowable range in a given condition in a large grain, i.e., a system without the grain boundary. In this study, we investigated the behavior of PDAS in the columnar dendrites growing between the diverging and converging grain boundaries by quantitative phase-field simulations. In the presence of grain boundaries, a new primary arm appear at the diverging grain boundary and a dendrite is eliminated at the converging grain boundary, leading to an almost uniform distribution of PDAS in the steady state. Importantly, the spatially averaged value of PDAS in the steady state is unique to a

given solidification condition. Such a unique value does not depend on the initial structure and thus on the history of solidification, which is in contrast to the existence of an allowable range of PDAS in a large grain. Moreover, this unique value decreases with an increase in V_p, and its dependence is consistent with the theoretical models. Furthermore, the dependence of the unique value on the inclination angle of crystals from the temperature gradient is well described by the model of Gandin et al. Note that the focus of the 2D and 3D simulations in this study is on the growth of columnar dendrites in a thin sample. A future investigation should be aimed at clarifying the existence of the unique value of PDAS in a bulk 3D system.

References

[1] W. Kurz and D.J. Fisher, Fundamentals of Solidification, Trans. Technol. Publications Ltd., Switzerland, 1989.

[2] D.A. Porter, K.E. Easterling and M.Y. Sherif, Phase Transformations in Metals and Alloys,CRC Press, United States, 1992.

[3] S. Ganesan, C. Chan and D. Poirier, Mat. Sci. Eng. A 151, (1992) 97-105.

[4] B. Goyeau, D. Gobin, T. Benihaddadene, D. Gobin and M. Quintard, Metall. Mater. Trans. B 30, (1999) 613-622.

[5] T. Takaki, S. Sakane, M. Ohno, Y. Shibuta and T. Aoki, Acta Mater. 164, (2019) 237-249.

[6] M.C. Scheneider and C. Beckermann, Int. J. Heat Mass Transf. 38, (1995) 3455-3473.

[7] H.J. Thevik and A. Mo, Int. J. Heat Mass Transf. 40, (1997) 2055-2065.

[8] M.L.N.M. Melo, E. Rizzo and R. Santos, J. Mater. Sci. 40, (2005) 1599-1609.

[9] J.D. Hunt, Solidification of Casting of Metals, The Metals Society, London, 1979.

[10] W. Kurz and D.J. Fisher, Acta Metall. 29, (1981) 11-20.

[11] R. Trivedi, Metall. Trans. A 15, (1984) 977-982.

[12] S.N. Tewari and V. Laxmanan, Acta Metall. 35, (1987) 175-183.

[13] J.A. Warren and J.S. Langer, Phys. Rev. A 42, (1990) 3518-3525.

[14] J.D. Hunt and S.Z. Lu, Metall. Mater. Trans. A 27, (1996) 611-623.

[15] H. Weidong, G. Xingguo and Z. Yaohe, J. Cryst. Growth 134, (1993) 105-115.

[16] G.L. Ding, W. Huang, X. Huang, X. Lin and Y.H. Zhou, Acta Mater. 44, (1996) 3705-3709.

[17] X. Lin, W. Huang, J. Feng, T. Li and Y. Zhou, Acta Mater. 47, (1999) 3271-3280.

[18] G. Kim, T. Takaki, Y. Shibuta, S. Sakane, K. Matsuura and M. Ohno, Comp. Mater. Sci. 162, (2019) 76-81.

[19] S. Gurevich, M.Amoorezaei and N. Provatas, Phys. Rev. E 82, (2010) 051606.

[20] S. Gurevich, A. Karma, M. Plapp and R. Trivedi, Phys. Rev. E 81, (2010) 011603.

[21] T. Takaki, M. Ohno, T. Shimokawabe and T. Aoki, Acta Mater. 81, (2014) 272-283.

[22] D. Tourret and A. Karma, Acta Mater. 82, (2015) 64-83.

[23] T. Takaki, S. Sakane, M. Ohno, Y. Shibuta, T. Shimokawabe and T. Aoki, Acta Mater. 118, (2016) 230-243.

[24] C. Yang, Q. Xu and B. Liu, J. Mater. Sci. 53, (2018) 9755-9770.

[25] Y. Song, S. Akamatsu, S. Bottin-Rousseau and A. Karma, Phys. Rev. Mater. 2, (2018) 053403.

[26] B. Echebarria, R. Folch, A. Karma and M. Plapp, Phys. Rev. E 70, (2004) 061604.

[27] M. Ohno and K. Matsuura, Phys. Rev. E 79, (2009) 031603.

[28] M. Ohno, T. Takaki and Y. Shibuta, Phys. Rev. E 93, (2016) 012802.

[29] M. Ohno, T. Takaki and Y. Shibuta, Phys. Rev. E 96, (2017) 033311.

[30] A. Karma and W.J. Rappel, Phys. Rev. E 60, (1999) 3614.

[31] A. Karma, Phys. Rev. Lett. 87, (2001) 115701.

[32] Y. Shibuta, M. Ohno and T. Takaki, JOM 67, (2015) 1793-1804.

[33] Y. Shibuta, M. Ohno and T. Takaki, Adv. Theory Simul. 1, (2018) 201800065.

[34] T. Takaki, T. Shimokawabe, M. Ohno, A. Yamanaka and T. Aoki, J. Cryst. Growth 382, (2013) 21-25.

[35] T. Takaki, S. Sakane, M. Ohno, Y. Shibuta, T. Aoki and C.A. Gandin, Materialia 1, (2018) 104-113.

[36] A.J. Clarke, D. Tourret, Y. Song, S.D. Imhoff, P.J. Gibbs, J.W. Gibbs, K. Fezzaa, A. Karma, Acta Mater. 129, (2017) 203-216.

[37] C.A. Gandin, M. Eshelman and R. Trivedi, Metall. Mater. Trans. A 27, (1996) 2727-2739.

[38] T. Takaki, M. Ohno, Y. Shibuta, S. Sakane, T. Shimokawabe and T. Aoki, J. Cryst. Growth 442, (2016) 14-24.

[39] K. Glasner, J. Comput. Phys. 174, (2001) 695-711.

[40] S.H. Park, H. Esaka and K. Shinozuka, J. JPN. Inst. Met. 76, (2012) 197-202.

[41] D. Tourret, Y. Song, A.J. Clarke, A. Karma, Acta Mater. 122, (2017) 220-235.

[42] C. Guo, J. Li, H. Yu, Z. Wang, X. Lin and J. Wang, Acta Mater. 136, (2018) 148-163.

Table 1

Input parameters [21, 23, 38].

Parameter	Symbol	Value
Liquid diffusivity	D_l	3.0×10^{-9} m^2/s
Solid diffusivity	D_s	3.0×10^{-13} m^2/s
Partition coefficient	k	0.14
Liquidus slope	m_l	-620.0 K per at. frac.
Gibbs-Thomson coefficient	Γ	0.24×10^{-6} Km
Melting temperature	T_m	933.25 K
Anisotropy coefficient	ε	0.02
Initial dimensionless supersaturation	u_0	-0.3
Interface thickness	W_0	$\Delta x/0.8 = 0.625$ μm
Reference temperature	T_0	922.39 K
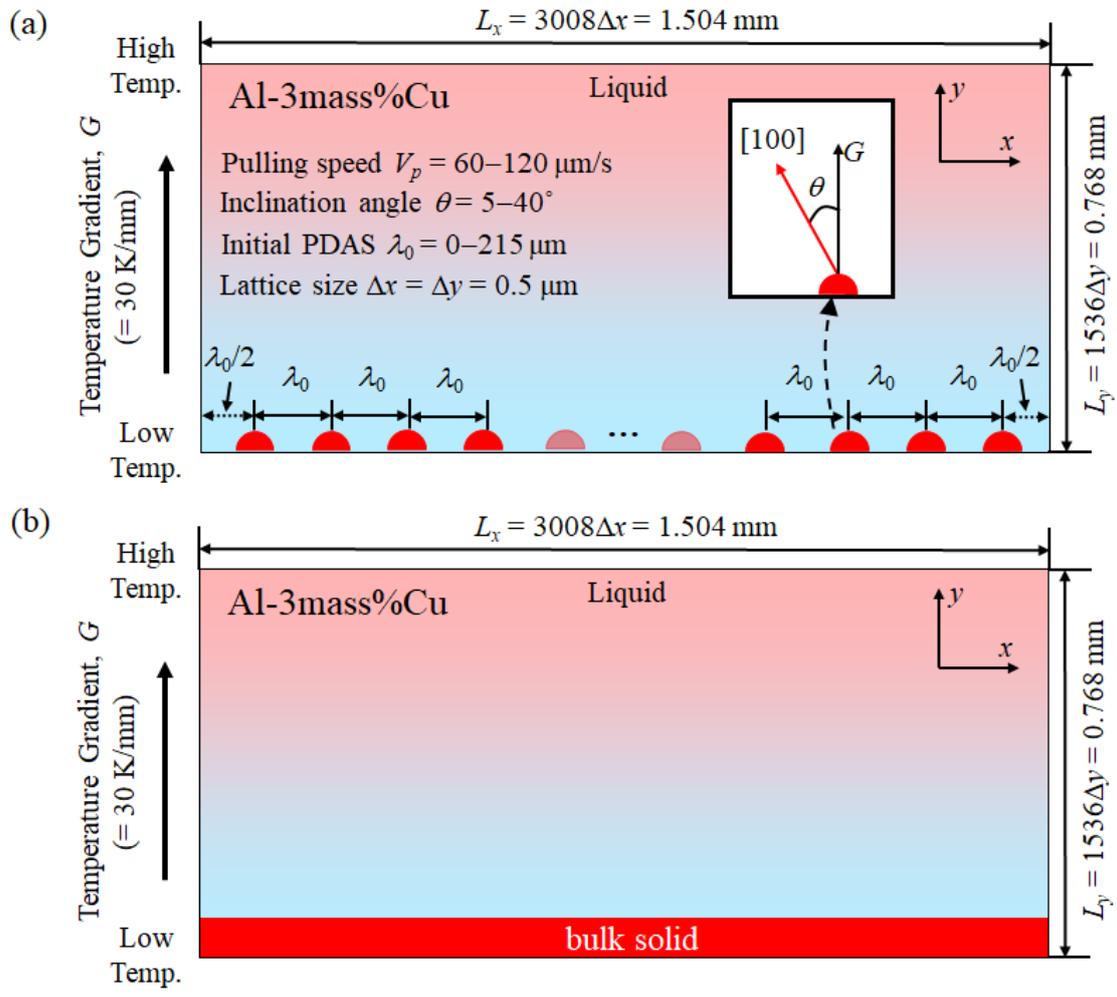
Fig. 1. The computational system and the initial condition for (a) $\lambda_0 > 0$ and (b) $\lambda_0 = 0$ μm which indicates the thin plate of bulk solid.
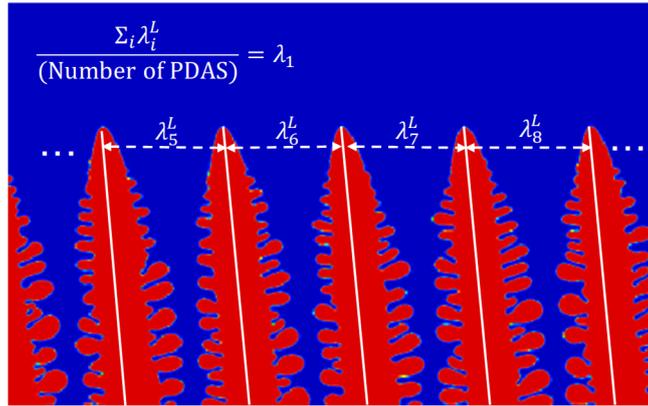
Fig. 2. A schematic illustration for the definition of PDAS. The position just below the tip of the dendrite is used for measuring the individual PDAS λ_i^L and the average PDAS λ_1.
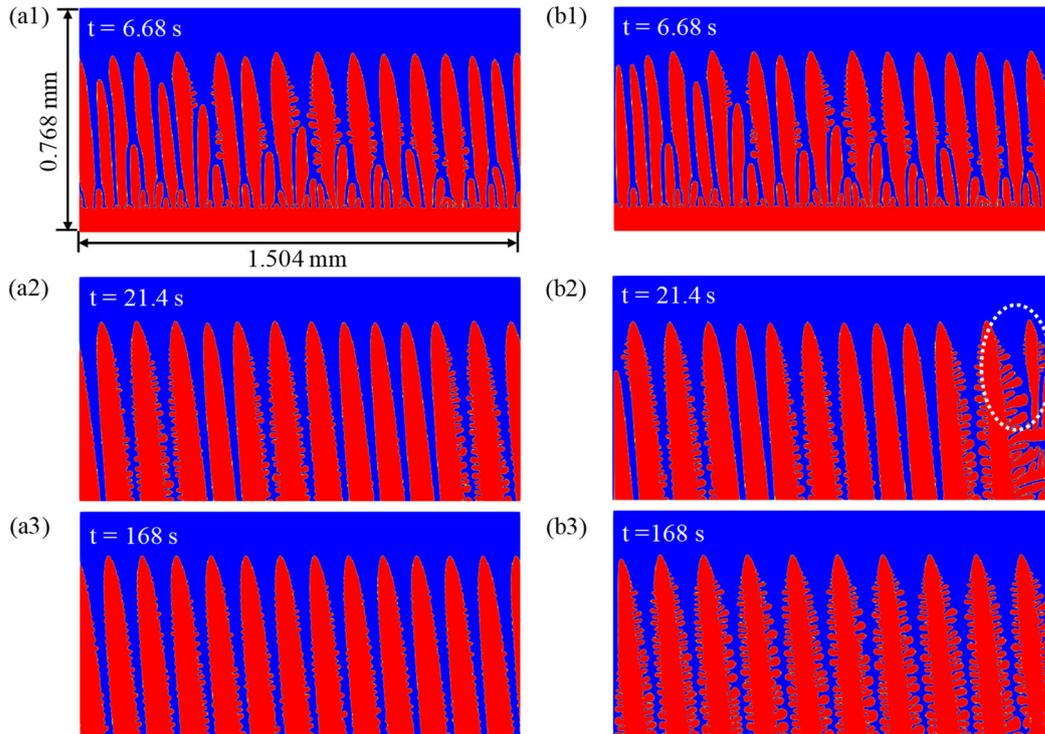
Fig. 3. Dendrite structures at $t = 6.68$ to 168 s for $V_p = 100$ μm/s, $\theta = 5°$, and $\lambda_0 = 0$ μm. Snapshots (a1)–(a3) show the results without the grain boundary (case 1), and those of (b1)–(b3) are the results with the grain boundaries (case 2). The dotted circle in (b2) indicates the occurrence of branching at the diverging grain boundary. The simulations were conducted for $L_x \times L_y = 1.536$ mm $\times$ 0.768 mm, $G = 30$ K/mm.
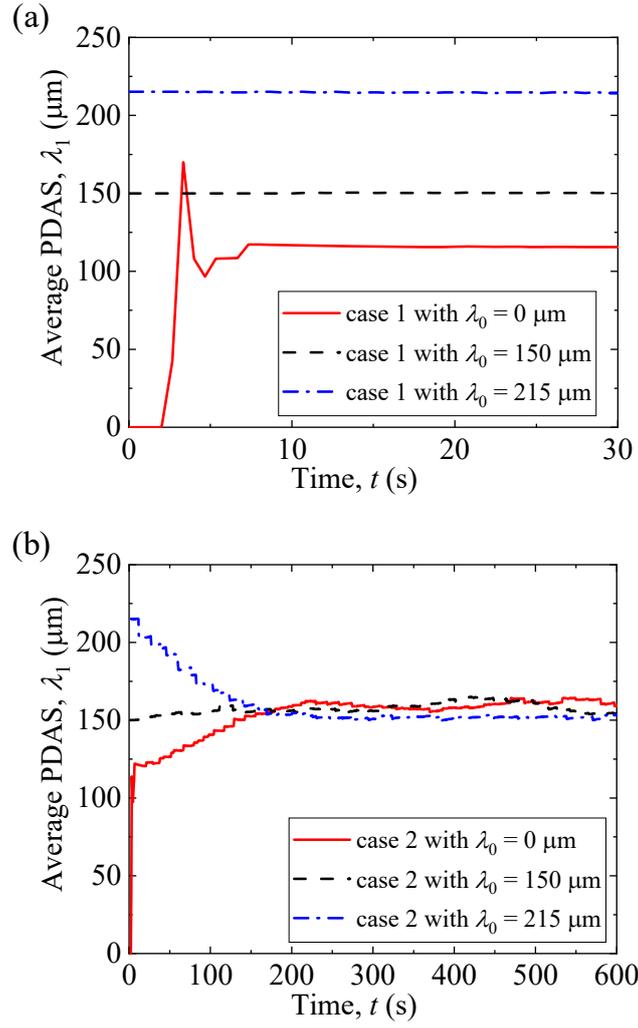
Fig. 4. Time dependence of λ_1 for (a) case 1 and (b) case 2 with different values of λ_0, calculated for $L_x \times L_y = 1.536$ mm$\times$0.768 mm, $V_p = 100$ μm/s, $G = 30$ K/mm, $\theta = 5°$.
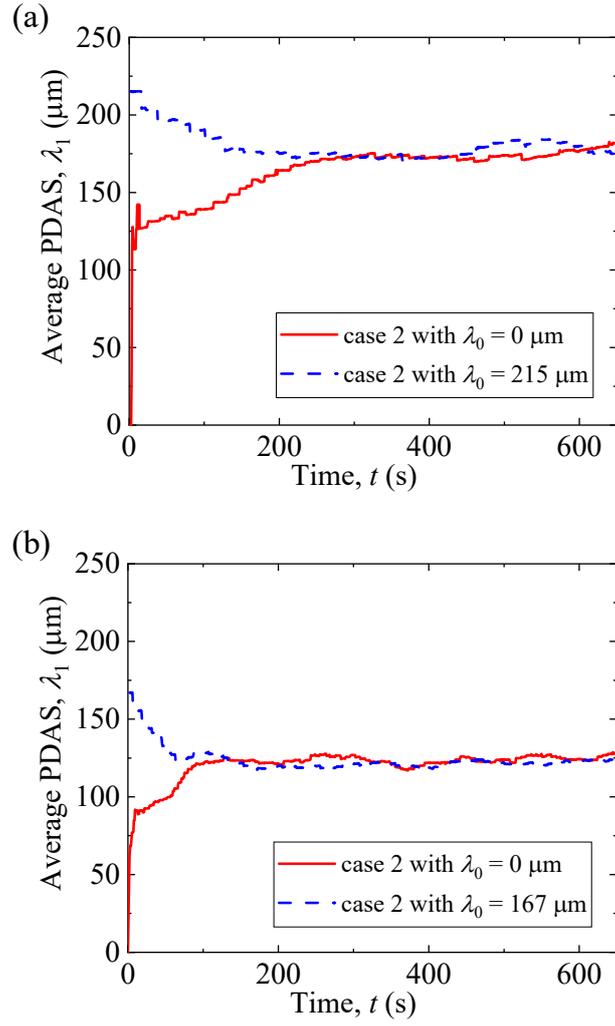
Fig. 5. Time dependence of λ_1 for (a) $V_p = 80$ μm/s and (b) $V_p = 200$ μm/s in case 2 with different values of λ_0, obtained for $L_x \times L_y = 1.536$ mm $\times$ 0.768 mm, $G = 30$ K/mm, $\theta = 5°$.
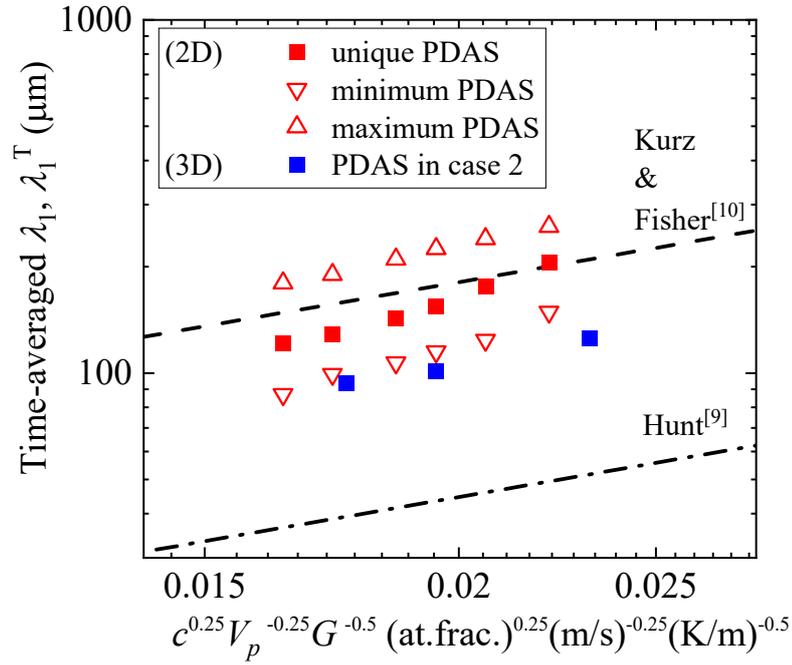
Fig. 6. Dependence of λ_1^T on the solidification for $\theta = 5°$. The triangle plots indicate the minimum and maximum values of λ_1^T in case 1 obtained from 2D phase-field simulations. The red- and blue-square plots represent the unique values of λ_1^T obtained from the 2D and 3D phase-field simulations, respectively, for case 2. The dotted and dash-dotted lines represent the results of the model by Kurz and Fisher [10] and Hunt [9], respectively.
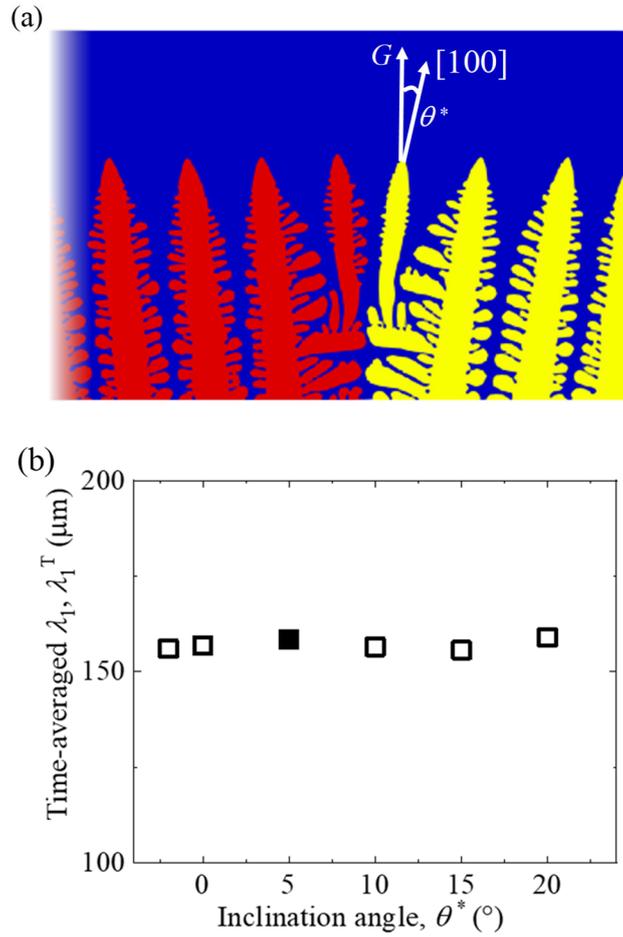
Fig. 7. Effect of the inclination angle of the competing dendrite (θ^*) in case 3. (a) Dendrite structure around the asymmetric diverging grain boundary. (b) Dependence of λ_1^T on θ^*, where the black-colored plot indicates the result obtained by using the mirror boundary conditions (symmetric diverging grain boundary). There were calculated for $L_x \times L_y = 2.8$ mm $\times 0.768$ mm, $V_p = 100$ μm/s, $G = 30$ K/mm, $\theta = 5°$ $\lambda_0 = 200$ μm.

(a)

(b)

(c)
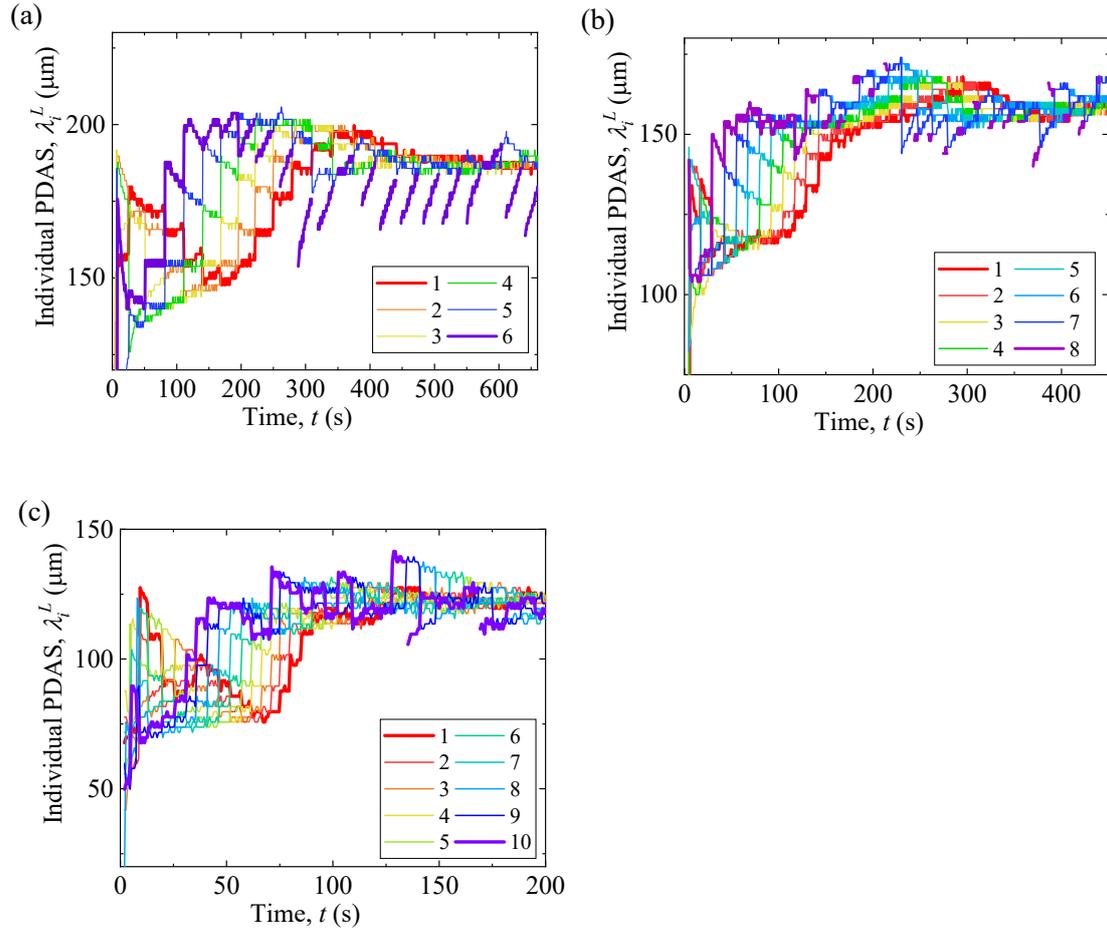
Fig. 8. Time variation of individual PDAS λ_i^L for $\theta = 5°$ and $\lambda_0 = 0$ μm in case 2 with $V_p =$ (a) 60 μm/s, (b) 100 μm/s, and (c) 200 μm/s. All λ_i^L formed by dendrites that exist up to the steady state (500, 200, and 150 s for (a), (b), and (c)) are numbered in order from the converging to the diverging grain boundary; that is, the number in the legend represents i for λ_i^L. The bold red line indicates λ_i^L nearest the converging grain boundary, whereas the bold purple line indicates λ_i^L nearest the diverging grain boundary. These results were obtained for $L_x \times L_y = 1.536$ mm $\times 0.768$ mm, $G = 30$ K/mm, $\lambda_0 = 0$ μm in case 2.
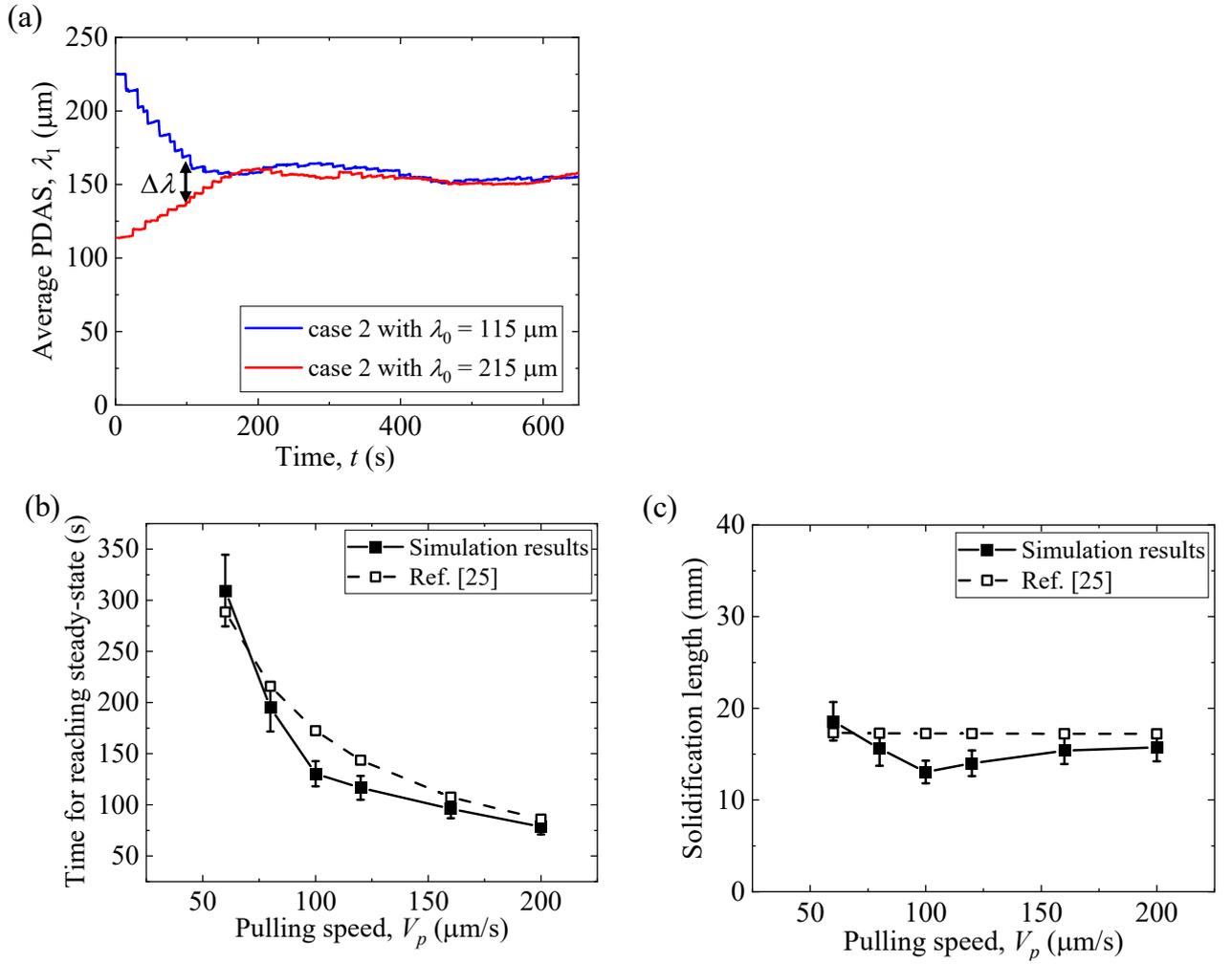
Fig. 9. (a) Time change of λ_1 for $\lambda_0 = 115$ and 225 μm, $V_p = 100$ μm/s, $\theta = 5°$. (b) solidification time and (c) solidification length to reach the steady state, calculated for different values of V_p. In Fig. (b) and (c), the filled square plots are the results of the phase-field simulation and the error bars represent the values for $\Delta\lambda = 5$ and 20 μm. The open square plots are the result of Eq. (4) [25]. These are obtained for $L_x \times L_y = 1.536$ mm$\times 0.768$ mm, $G = 30$ K/mm, $\lambda_0 = 87$ - 215 μm in case 2.
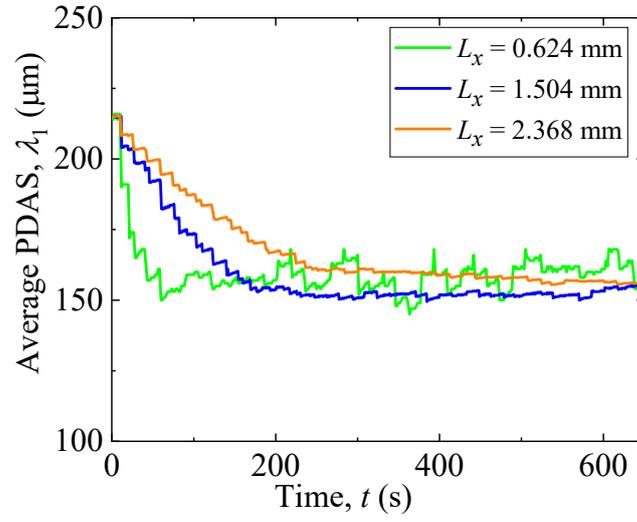
Fig. 10. Time dependence of λ_1 for $V_p = 100$ μm/s, $\theta = 5°$, and $\lambda_0 = 215$ μm with different widths of columnar grain. These results are obtained for $L_x \times L_y = (0.624 - 2.368)$ mm $\times 0.768$ mm, $V_p = 100$ μm/s, $G = 30$ K/mm, $\theta = 5°$, $\lambda_0 = 215$ μm in case 2.
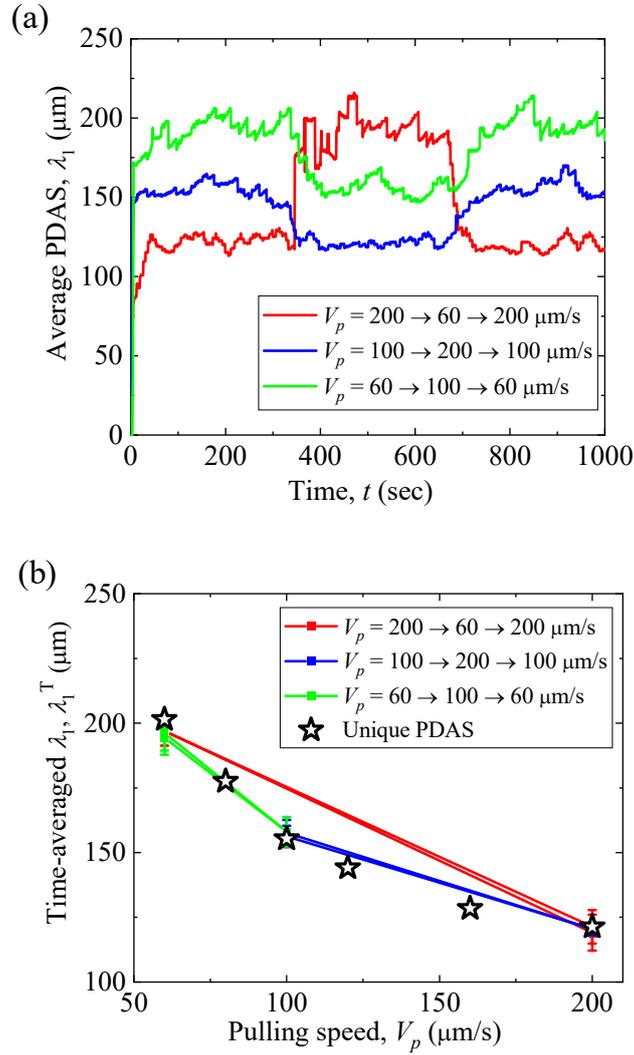
Fig. 11. (a) Time change of λ_1 associated with the rapid change in V_p calculated for $\theta = 5°$, $\lambda_0 = 0$ μm, $L_x = 0.768$ mm. (b) Dependence of λ_1^{T} on V_p. These results were obtained for $L_x \times L_y = 0.768$ mm $\times$ 0.768 mm, $G = 30$ K/mm, $\theta = 5°$ and $\lambda_0 = 0$ μm in case 2.
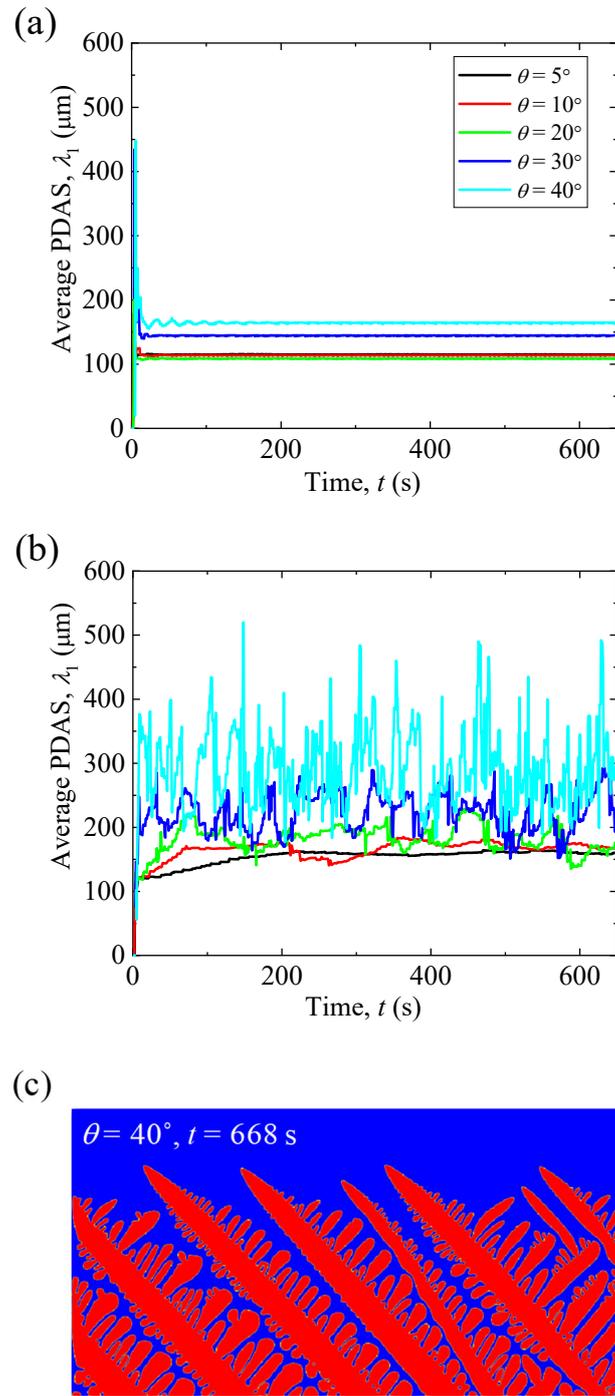
Fig. 12. Time dependence of PDAS for different values of θ in (a) cases 1 and (b) 2. (c) A snapshot of dendrites at 668 s and $\theta = 40°$ in case 2. These results were obtained for $L_x \times L_y = 1.536$ mm $\times 0.768$ mm, $V_p = 100$ μm/s, $G = 30$ K/mm, $\lambda_0 = 0$ μm in cases 1 and 2.
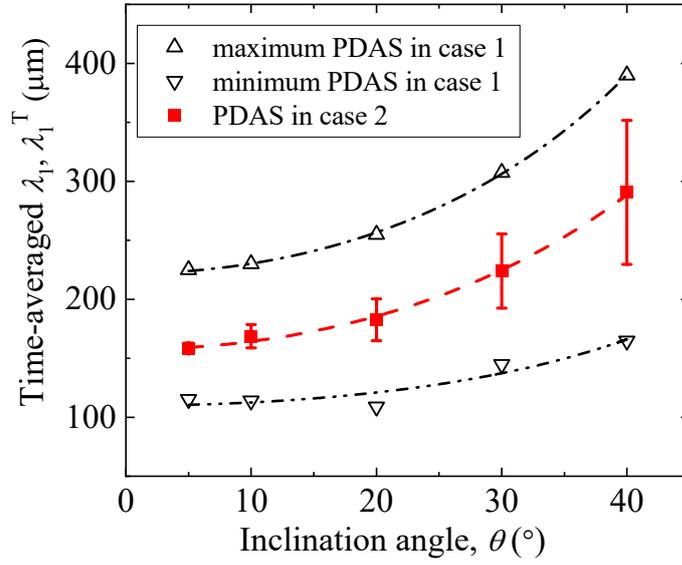
Fig. 13. Dependence of λ_1^T on θ in cases 1 and 2. The red-colored dashed line, dashed dot line, and dashed two-dot lines are drawn by fitting the model of Gandin et al. [36] to the results of the phase-field simulations. These results were obtained for $L_x \times L_y$ = 1.536 mm $\times$ 0.768 mm, V_p = 100 μm/s, G = 30 K/mm, λ_0 = 0 - 390 μm in cases 1 and 2.
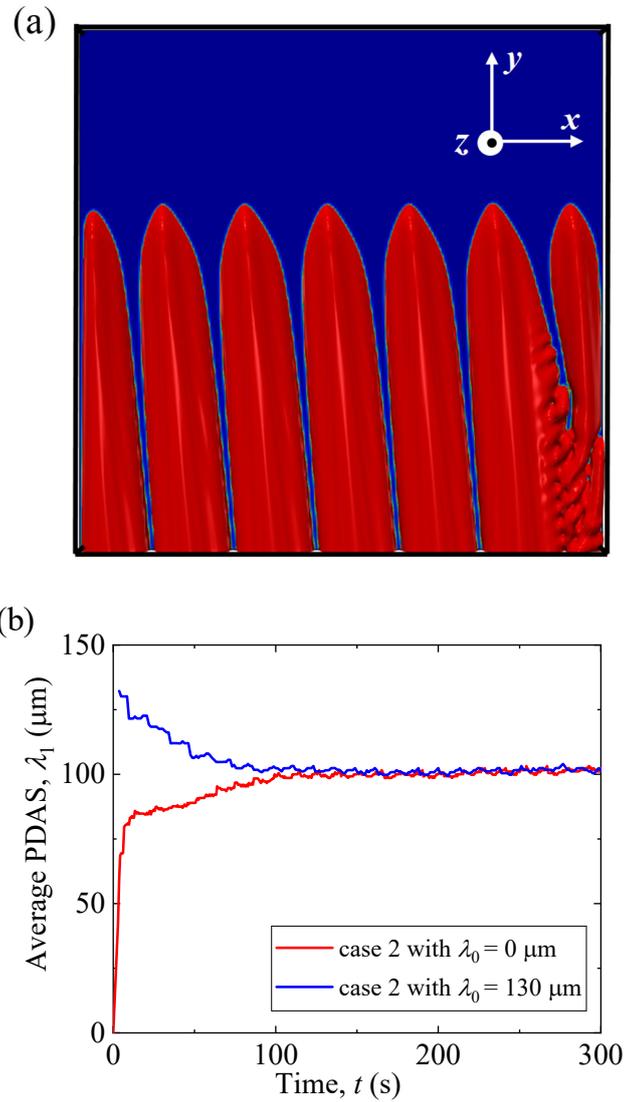
Fig. 14. Investigation on the 3D system. (a) The morphology of dendrites calculated for $V_p = 100$ μm/s and $\theta = 5°$ at 270 s observed in directions of z (above) and y (below). (b) Time variation of λ_1 in case 2 with $\lambda_0 = 0$ and 130 μm. The results were obtained for $L_x \times L_y \times L_z = 0.640$ mm $\times 0.640$ mm $\times 0.032$ mm, $G = 30$ K/mm in case 2.